Mesoscopic Transport in Electrostatically Defined Spin-Full Channels in Quantum Hall Ferromagnets

Aleksandr Kazakov,[1] George Simion,[1] Yuli Lyanda-Geller,[1,2] Valery Kolkovsky,[3] Zbigniew Adamus,[3] Grzegorz Karczewski,[3] Tomasz Wojtowicz,[3,4] and Leonid P. Rokhinson[1,2,5,*]

[1]*Department of Physics and Astronomy, Purdue University, West Lafayette, Indiana 47907, USA*
[2]*Birck Nanotechnology Center, Purdue University, West Lafayette, Indiana 47907, USA*
[3]*Institute of Physics, Polish Academy of Sciences, Aleja Lotnikow 32/46, PL-02668 Warsaw, Poland*
[4]*International Research Centre MagTop, Aleja Lotnikow 32/46, PL-02668 Warsaw, Poland*
[5]*Department of Electrical and Computer Engineering, Purdue University, West Lafayette, Indiana 47907, USA*

(Received 10 February 2017; published 25 July 2017)

In this work, we use electrostatic control of quantum Hall ferromagnetic transitions in CdMnTe quantum wells to study electron transport through individual domain walls (DWs) induced at a specific location. These DWs are formed due to the hybridization of two counterpropagating edge states with opposite spin polarization. Conduction through DWs is found to be symmetric under magnetic field direction reversal, consistent with the helical nature of these DWs. We observe that long domain walls are in the insulating regime with a localization length of 4–6 μm. In shorter DWs, the resistance saturates to a nonzero value at low temperatures. Mesoscopic resistance fluctuations in a magnetic field are investigated. The theoretical model of transport through impurity states within the gap induced by spin-orbit interactions agrees well with the experimental data. Helical DWs have the required symmetry for the formation of synthetic p-wave superconductors. The achieved electrostatic control of a single helical domain wall is a milestone on the path to their reconfigurable network and ultimately to a demonstration of the braiding of non-Abelian excitations.

DOI: 10.1103/PhysRevLett.119.046803

The prediction that one-dimensional (1D) wires with lifted Kramers degeneracy but preserved time-reversal symmetry coupled to a conventional superconductor can harbor non-Abelian excitations [1] motivated the development of various systems with conducting 1D helical channels. The required symmetry has been predicted [2,3] and demonstrated in nanowires with strong spin-orbit interaction in the presence of a magnetic field [4–6], at the edges of the quantum spin Hall effect devices [7], and in atomic chains with a helical magnetic structure [8]. None of the aforementioned systems are easily reconfigurable, which hinders the demonstration of braiding of quasiparticles and non-Abelian statistics.

Edge states in the quantum Hall effect (QHE) regime have been used as a canonical system to study 1D Luttinger liquids [9], which are *chiral* and not time-reversal invariant. However, there is one overlooked regime in the QHE, the quantum Hall ferromagnetic (QHFM) transition—where *helical* channels can be formed. The spin polarization of the topmost Landau level is determined by a competition between Zeeman, cyclotron, and exchange energies. Changing the balance between these energies (e.g., by applying an in-plane magnetic field) can lead to a QHFM transition where a uniform 2D gas spontaneously phase separates into regions with different spin polarizations [10]. Domain walls at the boundaries of insulating ferromagnetic domains form helical 1D channels (HDWs) [11–15], and transport through a random network of conducting DWs has been studied in the context of a 2D phase transition [16–18]. In the past, the study of an individual HDW was not feasible. In this Letter, we use the recently developed gate control of the QHFM transition [19] in CdMnTe quantum wells to demonstrate that HDWs can be formed at a specific location using electrostatic gating, and we also present an investigation of transport properties of isolated HDWs.

The QHFM transition was first observed at a filling factor $\nu = 2/3$ [20] in high-mobility GaAs quantum wells. In this Letter, we focus on the QHFM transition at $\nu = 2$ in CdMnTe dilute magnetic semiconductor quantum wells [21], where QHFM transitions in both integer [17] and fractional [22] QHE regimes have been observed. The QHFM transition in CdMnTe originates from a competition between negative Zeeman energy (the Landé g factor of CdTe $g = -1.6$) and positive exchange energy between s electrons in the quantum well and d-shell electrons in Mn. The presence of the $s-d$ exchange modifies Landau levels [see Fig. 1(a)] and can result in the crossing of levels with different polarizations at high magnetic fields. The magnetic field B^* corresponds to a cancellation of differences in the total Zeeman, cyclotron, and exchange energies of $|0\uparrow\rangle$ and $|1\downarrow\rangle$ states. At this field, levels would cross, but a spin-orbit interaction introduces a small avoided crossing [19]. When driven through B^*, the 2D gas undergoes a polarized ($\downarrow\downarrow$) to unpolarized ($\downarrow\uparrow$) phase transition at $\nu = 2$ (only two Landau levels filled), which is marked on the

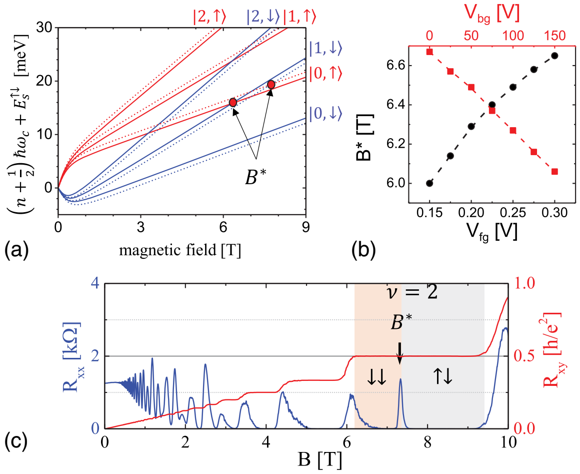

FIG. 1. (a) Calculated energy spectrum of Landau levels in CdMnTe with 1.7% Mn doping and $s-d$ overlap $0.9\chi_0$ (solid lines) and $1.1\chi_0$ (dashed lines), where χ_0 is the overlap for zero gate voltages. B^* marks QHFM transitions where the ground state changes from $|0\uparrow\rangle$ to $|1\downarrow\rangle$. (b) Experimentally measured shift of QHFM at $\nu = 2$ as a function of front (V_{fg}) and back (V_{bg}) gate voltages. (c) Longitudinal and Hall resistance measured at an elevated temperature of 300 mK. The sharp peak at 7.3 T within the $\nu = 2$ shaded region is a QHFM transition between fully polarized and unpolarized states, where the top filled Landau level changes polarization.

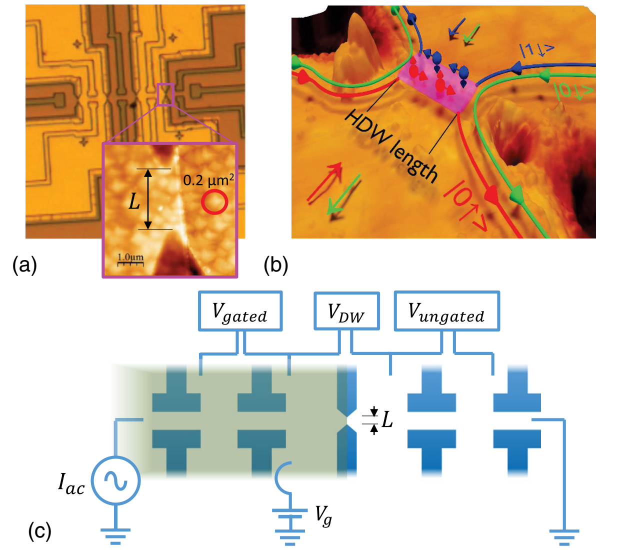

FIG. 2. (a) Optical image of a sample; dark areas are etched, and yellow areas are covered by a top gate. The inset is an AFM image of a constriction, where the vertical gate boundary is clearly seen. (b) An artistic rendering of an AFM image at $\nu = 2$ with a schematic flow of $|0\uparrow\rangle$, $|0\downarrow\rangle$, and $|1\downarrow\rangle$ edge channels assuming that the QHFM transition is gate tuned across the constriction. $|0\uparrow\rangle$ and $|1\downarrow\rangle$ states hybridize forming a helical domain wall. (c) Schematic of the measurement setup.

plot. We observe that in transport this QHFM transition is seen as a sharp peak in the longitudinal resistance in the middle of the $\nu = 2$ plateau [Fig. 1(c)].

Electrostatic control of the QHFM transition in CdMnTe was developed in Ref. [19], where we introduced nonuniform placement of Mn in the growth direction within the quantum well. The electric field shifts the electron wave function relative to the Mn position, thereby controlling the $s-d$ overlap $\chi(V_g)$. The corresponding change in the strength of the $s-d$ exchange results in the shift of B^*, as shown for two values of χ in Fig. 1(a). Experimentally, we can control B^* within ~10% by both front and back gates as shown in Fig. 1(b).

Devices were fabricated from CdMnTe/$Cd_{0.8}Mg_{0.2}Te$ quantum well (QW) heterostructures grown by molecular beam epitaxy; see Refs. [17,22] for details. The QW is 30 nm wide and is modulation doped with iodine. Mn is introduced into the QW as seven δ-doping layers spaced by six monolayers of CdTe starting 13 nm from the bottom of the quantum well in the growth direction. The effective Mn concentration is 1.5%–1.7% as determined from the position of the QHFM transition B^* at $\nu = 2$. The low-temperature density and mobility in ungated samples are $3\text{–}3.5 \times 10^{11}$ cm^{-2} and $3\text{–}4 \times 10^4$ cm^2/V s, respectively. The transition field B^* at zero gate voltage can be adjusted by varying conditions of the LED illumination during a cooldown [23]. We attribute this tunability to different dopant ionization profiles and, consequently, different profiles of the electron wave function within the quantum well. A semitransparent front gate is formed by evaporating 10–15 nm of Ti on the surface of the sample, and a copper foil glued to the back of the sample serves as a back gate. Ohmic contacts are produced by soldering freshly cut indium pellets similar to previous studies [17,22]. Electron transport is measured in a dilution refrigerator in a temperature range 30–650 mK with a standard ac technique using excitation current $I_{\mathrm{ac}} \leq 1$ nA.

Samples are patterned in a number of gated and ungated Hall bar sections with sizes of 25 μm length and 15 μm width; see Fig. 2. The front gate boundary is aligned with narrow constrictions of various lithographical widths $L = 1\text{–}15\mu$m. The constrictions electrical width is reduced by $2l_D = 200\text{–}400$ nm, where l_D is the depth of electrical depletion of a 2D electron gas near the mesa edges. It is further reduced by $\approx 1.8 l_D - 2.5\sqrt{a_B l_D} = 120\text{–}280$ nm ($a_B = 5.4$ nm is the Bohr radius in CdTe) due to the formation of edge channels in the QHE regime [26]. The overall reduction is 0.5–1 μm compared to the lithographic L. This sample design allows the simultaneous measurement of longitudinal resistance $R_{xx} = V_{xx}/I_{\mathrm{ac}}$ in gated (R_{gated}) and ungated (R_{ungated}) regions, as well as longitudinal resistance in the presence of the domain wall R_{DW} [Fig. 2(c)].

The difference between QHFM transitions in gated and ungated regions is $\Delta B^* = B^*_{\mathrm{ungated}} - B^*_{\mathrm{gated}}$, and positions of B^* within $\nu = 2$ plateaus can be adjusted by a combination of cooldown conditions and gate voltages [23]. Note that the energy gap in the vicinity of the QHFM transition is

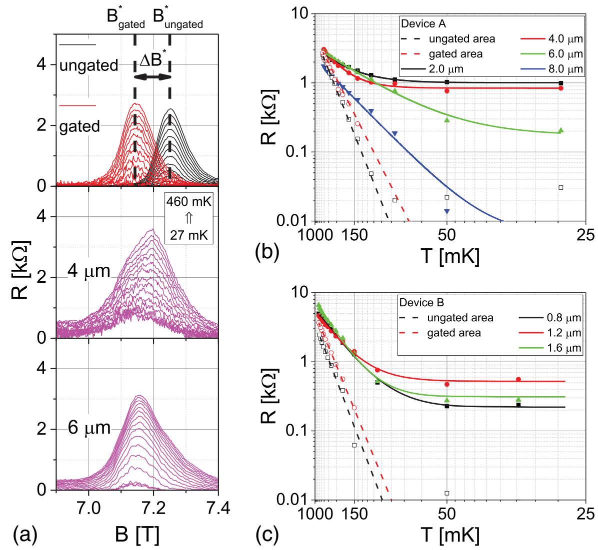

FIG. 3. (a) The upper panel shows QHFM transitions for large ungated and gated areas. R_{DW} for $L = 4$ and 6 μm constrictions is plotted in the lower panels. Dashed lines mark B^* in gated and ungated areas. At low temperatures, the resistance of the $L = 6$ μm constriction almost vanishes, while for $L = 4$ μm it saturates to a nonzero value. (b),(c) $R_{DW}(T)$ dependence for constrictions with different L for $\Delta B^* = 0.11$ T in device A and $\Delta B^* = 0.25$ T in device B are plotted in an Arrhenius plot. Solid lines are fits to $R = R_0 + Ae^{-E_a/kT}$, and dashed lines are fits to thermally activated conduction with a gap ≈1 K.

$\sim\hbar e|\Delta B^*|/2m = \hbar\Delta\omega_c/2 \approx 0.57$ meV/T and increases with separation ΔB^*. The value ΔB^* controls the gradient of the $s - d$ exchange and the width of the HDWs and can be adjusted between 0 and 0.3 T in our experiments.

The magnetoresistance in the vicinity of the QHFM transition for $\Delta B^* = 0.11$ T, where both $B^*_{\rm gated} = 7.14$ T and $B^*_{\rm ungated} = 7.25$ T are tuned into the middle of the $\nu = 2$ plateau, is plotted in Fig. 3. Here $\nu = 2$ extends between 6.7 and 8.2 T. $R_{xx} = 0$ below 7.0 T corresponds to a fully polarized ($\downarrow\downarrow$) state with the $|1\downarrow\rangle$ topmost energy level filled, while $R_{xx} = 0$ above 7.4 T is an unpolarized ($\downarrow\uparrow$) state with the topmost energy level $|0\uparrow\rangle$. Resistance of the QHFM transition peak for wide 2D regions shows activation behavior with an energy gap ≈1 K; see the dashed lines in Figs. 3(b) and 3(c) attributed to spin-orbit coupling of $|1\downarrow\rangle$ and $|0\uparrow\rangle$ Landau levels [19]. The value of ΔB^* is large enough that the resistance in the midpoint $B = 7.195$ T vanishes at low $T < 100$ mK. Thus, the QHFM transition at a gate boundary should occur in the range 7.14 T $< B <$ 7.25 T. Indeed, R_{DW} peaks within that field range as shown in the middle and bottom panels in Fig. 3(a). For narrow (short) constrictions, $L < 6$ μm, the resistance saturates at low temperatures to a nonzero value; see Figs. 3(b) and 3(c). It is important to note that for $T < 100$ mK the contribution of the wide 2D regions to R_{DW} is negligible, and R_{DW} originates from the conduction through the channel formed along the gate boundary.

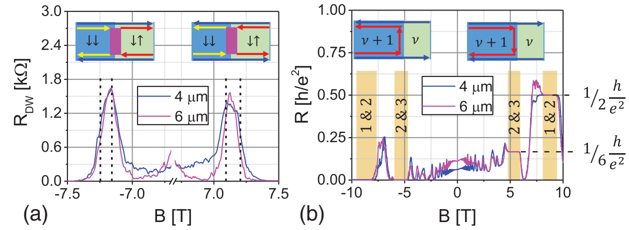

FIG. 4. (a) The resistance of the HDW is symmetric under magnetic field reversal. (b) In the presence of chiral channels formed at a boundary between two different QHE states, the resistance is highly asymmetric under magnetic field reversal (highlighted regions are for the boundaries between $\nu = 1$ and 2 and 2 and 3 QHE states).

One of the hallmarks of time-reversal-invariant *helical* DWs is the symmetry with respect to magnetic field reversal, because domain walls emerge from two counter-propagating edges with the same filling factor. Indeed, we observed that $R_{DW}(B) \approx R_{DW}(-B)$; see Fig. 4(a). This magnetic field reversal symmetry is in striking contrast to properties of $R = R_{ch}$ measured when a *chiral* channel is formed at a boundary of ν and $\nu + 1$ QHE states, where $R_{ch} = 0$ for one field direction and $R_{ch} = \{(1/\nu) - [1/(\nu + 1)]\}^{-1}\ h/e^2$ for the other direction [27]. Indeed, at positive B, we see $R_{ch} = h/2e^2$ at the boundary between $\nu = 1$ and $\nu = 2$ and $R_{ch} = h/6e^2$ at the boundary between $\nu = 2$ and $\nu = 3$. However, with reversed B at the same boundaries, $R_{ch} = 0$ [Fig. 4(b)].

Helical domain walls are formed by two counterpropagating edge channels along the gate boundary with opposite spin orientations. The measured values of $R_{DW} < 1$ kΩ. This demonstrates that counterpropagating edge channels at the same ν cannot be in the regime of ballistic transport, as this would result in $R_{DW} = h/2e^2 = 12.9$ kΩ, inconsistent with experimental observations. In order to quantify transport characteristics of HDW, we describe them as resistors r which connect $\nu = 2$ edge states on the opposite sides of a constriction, as shown schematically in Fig. 2(b). The resistance r is defined by the voltage drop along the length of the domain wall as current flows in the same direction. This direction is perpendicular to the direction of the change of spin polarization caused by the electrostatic gate (Fig. 2). Assuming there is no equilibration between $\nu = 1$ and $\nu = 2$ edge channels, within the Landauer-Büttiker formalism we obtain $R_{DW} = 1/(4r + 6)$ [23]. For all r, in this model $R_{DW} < 1/6h/e^2 = 4.3$ kΩ, consistent with measured values of R_{DW}.

Certain insight into the nature of the electronic transport through HDWs can be obtained from mesoscopic fluctuations observed at low temperatures. As shown in Fig. 5(a), in short HDWs quasiperiodic conductance fluctuations are clearly seen. The quasiperiod ΔB of these oscillations is ~40–55 mT. Similar quasiperiodic resistance fluctuations were observed in mesoscopic devices for transitions

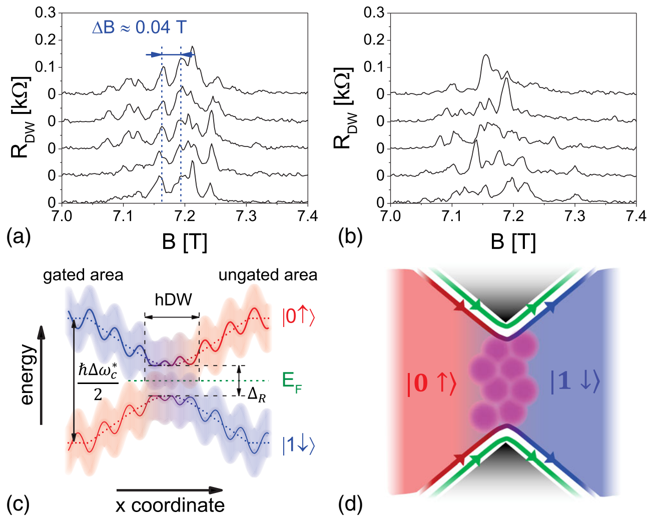

FIG. 5. (a),(b) Mesoscopic fluctuations measured in a device with $L = 2\ \mu$m constriction at $T = 27$ mK. In (a), the magnetic field was swept within the $\nu = 2$ state 6.8–7.5 T. Fluctuations have a similar pattern with a quasiperiod of $\Delta B \sim 40$ mT. In (b), B was changed in a wide range of 5–10 T, and the fluctuation pattern changes drastically. (c) Energy diagram of a HDW formed at the gate boundary. Wiggling lines indicate schematically the role of disorder, and shaded areas are localized states in the tails of Landau levels. At low temperatures, conduction occurs via localized states in the gap. (d) Schematic of a conducting channel formed by coupled $\nu = 2$ edge states. Electron tunneling via magenta in-gap states provide several interfering trajectories resulting in mesoscopic fluctuations of resistance.

between neighboring quantum Hall states [28,29]. From the exponential decay of the fluctuation's amplitude, we estimate the phase coherence length $l_\phi \propto T^{-1} \sim 1$–$2\ \mu$m at the base temperature [23], comparable with the length of the HDWs. One possible interpretation of mesoscopic fluctuations is the formation of a multidomain structure with a small network of HDWs spanning across the constriction. On the one hand, some static disorder, such as Mn doping fluctuations, potential fluctuations due to remote impurities, or surface roughness with a characteristic size of 0.2 μm [see the atomic force micrograph of the device surface in Fig. 2(a)] which results in a fluctuation of the perpendicular component of the magnetic field, may act as pinning centers for domain formation. On the other hand, experimentally we found that the fluctuation pattern changes drastically every time the magnetic field is ramped outside the $\nu = 2$ state [Fig. 5(b)], which means that dynamic fluctuations rather than static impurities define the conduction path within the channel. This conclusion is further supported by the observation that the fluctuation pattern slowly changes over several hours even if the field is kept close to the QHFM transition [23]. We also note that the width of the gate-defined potential gradient, which coincides with the region of $s - d$ exchange gradient and defines the width of the conductive channel, is of the order of the 2D gas-to-gate distance ($\approx$100 nm), similar to the expected width of HDWs defined by the spin-orbit coupling and a gradient of exchange interaction. Thus, the formation of a multidomain structure is highly unlikely. Assuming the width of the HDW to be $\sim$100 nm, the period of quasiperiodic oscillations is close to the area of a single HDW formed in a $L = 2\ \mu$m constriction.

In long channels $L > 6\ \mu$m, we observed the suppression of conduction at low temperatures. Similarly to the bulk Landau levels, edge states with spins $|0\uparrow\rangle$ and $|1\downarrow\rangle$ do not cross and exhibit a spin-orbit gap $\Delta_R \approx 50\ \mu$eV. Electron states in the gap in long channels become localized, i.e., strongly decay on the scale of the length of constriction $L > 6\ \mu$m. Thus, transport thermally activated over the gap is a dominant mechanism of conduction in such channels. In short $L < 4\ \mu$m HDWs, in-gap states should provide a conduction path at low temperatures. The in-gap states are due to charge defects binding electrons in the tail of Landau levels. This is consistent with the experimental observation that large changes in the magnetic field (i.e., the shift of Landau levels relative to the Fermi energy) alter the interference pattern. This model is visualized in Fig. 5(c), where the anticrossing of broadened Landau levels with in-gap states at the Fermi level is shown schematically to form a single HDW. Within this picture, transport through a single HDW can be modeled numerically; see Supplemental Material [23] for details. In the model, we assume that the primary source of localized states in the spin-orbit gap are potential fluctuations due to the remote doping, and we use the zero-field mobility to calculate the strength and density of the fluctuations. We also include surface roughness, which leads to the deviation of magnetic field orientation and orientation of Mn spins from the z direction at high fields, effectively introducing a magnetic disorder. The calculated conductance of a HDW is $1/r = 0.146 \pm 0.026 e^2/h$, which corresponds to $R_{\mathrm{DW}} = 0.66$–0.87 kΩ, in good agreement with the experiment. Modeling also confirms that transport is indeed dominated by the conduction via in-gap states. The calculated HDW resistance yields resistance R_{DW} symmetric under magnetic field reversal.

In conclusion, we demonstrated a conducting helical domain wall electrostatically defined at a designed location and studied its transport properties. We have found that long $L > 6\ \mu$m HDWs are insulating at low temperatures, consistent with the activation behavior of the QHFM transition in the bulk. Short $L < 6\ \mu$m HDWs remain conducting even at low temperatures. We find that conduction in short HDWs occurs via in-gap states, and conduction is symmetric under magnetic field reversal, a hallmark of helical channels. These HDWs, coupled to an s-wave superconductor, should support non-Abelian excitations. The investigated electrostatic control of HDW formation and transport provides a mechanism to form a reconfigurable network of helical channels and is an important milestone toward the realization of braiding of non-Abelian excitations.

The authors acknowledge support by the Department of Defense Office of Naval research Grant No. N00014 1410339 (A. K., T. W., G. S., Y. L-G., and L. P. R.), by the National Science Centre (Poland) Grant No. DEC-2012/06/A/ST3/00247 (V. K., Z. A., G. K., and T. W.), and by the Foundation for Polish Science through the IRA Program financed by EU within SG OP (T. W.).

*leonid@purdue.edu

[1] A. Kitaev, Phys. Usp. **44**, 131 (2001).
[2] R. M. Lutchyn, J. D. Sau, and S. Das Sarma, Phys. Rev. Lett. **105**, 077001 (2010).
[3] Y. Oreg, G. Refael, and F. von Oppen, Phys. Rev. Lett. **105**, 177002 (2010).
[4] L. P. Rokhinson, X. Liu, and J. K. Furdyna, Nat. Phys. **8**, 795 (2012).
[5] A. Das, Y. Ronen, Y. Most, Y. Oreg, M. Heiblum, and H. Shtrikman, Nat. Phys. **8**, 887 (2012).
[6] H. O. H. Churchill, V. Fatemi, K. Grove-Rasmussen, M. T. Deng, P. Caroff, H. Q. Xu, and C. M. Marcus, Phys. Rev. B **87**, 241401(R) (2013).
[7] M. König, S. Wiedmann, C. Brüne, A. Roth, H. Buhmann, L. W. Molenkamp, X.-L. Qi, and S.-C. Zhang, Science **318**, 766 (2007).
[8] S. Nadj-Perge, I. Drozdov, J. Li, H. Chen, S. Jeon, J. Seo, A. MacDonald, B. Bernevig, and A. Yazdani, Science **346**, 602 (2014).
[9] X. G. Wen, Phys. Rev. B **41**, 12838 (1990).
[10] B. Verdene, J. Martin, G. Gamez, J. Smet, K. von Klitzing, D. Mahalu, D. Schuh, G. Abstreiter, and A. Yacoby, Nat. Phys. **3**, 392 (2007).
[11] V. I. Fal'ko and S. V. Iordanskii, Phys. Rev. Lett. **82**, 402 (1999).
[12] T. Jungwirth and A. H. MacDonald, Phys. Rev. Lett. **87**, 216801 (2001).
[13] J. T. Chalker, D. G. Polyakov, F. Evers, A. D. Mirlin, and P. Wölfle, Phys. Rev. B **66**, 161317(R) (2002).
[14] L. Brey and C. Tejedor, Phys. Rev. B **66**, 041308 (2002).
[15] A. Mitra and S. M. Girvin, Phys. Rev. B **67**, 245311 (2003).
[16] E. De Poortere, E. Tutuc, J. Papadakis, and M. Shayegan, Science **290**, 1546 (2000).
[17] J. Jaroszyński, T. Andrearczyk, G. Karczewski, J. Wróbel, T. Wojtowicz, E. Papis, E. Kamińska, A. Piotrowska, D. Popović, and T. Dietl, Phys. Rev. Lett. **89**, 266802 (2002).
[18] F. J. Teran, M. Potemski, D. K. Maude, T. Andrearczyk, J. Jaroszyński, T. Wojtowicz, and G. Karczewski, Phys. Rev. B **82**, 245120 (2010).
[19] A. Kazakov, G. Simion, Y. Lyanda-Geller, V. Kolkovsky, Z. Adamus, G. Karczewski, T. Wojtowicz, and L. P. Rokhinson, Phys. Rev. B **94**, 075309 (2016).
[20] J. P. Eisenstein, H. L. Stormer, L. N. Pfeiffer, and K. W. West, Phys. Rev. B **41**, 7910 (1990).
[21] T. Wojtowicz, M. Kutrowski, G. Karczewski, J. Kossut, B. König, A. Keller, D. Yakovlev, A. Waag, J. Geurts, W. Ossau, G. Landwehr, I. Merkulov, F. Teran, and M. Potemski, J. Cryst. Growth **214–215**, 378 (2000).
[22] C. Betthausen, P. Giudici, A. Iankilevitch, C. Preis, V. Kolkovsky, M. Wiater, G. Karczewski, B. A. Piot, J. Kunc, M. Potemski, T. Wojtowicz, and D. Weiss, Phys. Rev. B **90**, 115302 (2014).
[23] See Supplemental Material at http://link.aps.org/supplemental/10.1103/PhysRevLett.119.046803 for additional experiments and modeling details, which includes Refs. [24,25].
[24] G. Giuliani and G. Vignale, *Quantum Theory of the Electron Liquid* (Cambridge University Press, Cambridge, England, 2005).
[25] D. K. Ferry, S. M. Goodnick, and J. Bird, *Transport in Nanostructures* (Cambridge University Press, Cambridge, England, 2009).
[26] D. B. Chklovskii, B. I. Shklovskii, and L. I. Glazman, Phys. Rev. B **46**, 4026 (1992).
[27] R. J. Haug, Semicond. Sci. Technol. **8**, 131 (1993).
[28] J. K. Jain and S. A. Kivelson, Phys. Rev. Lett. **60**, 1542 (1988).
[29] J. A. Simmons, S. W. Hwang, D. C. Tsui, H. P. Wei, L. W. Engel, and M. Shayegan, Phys. Rev. B **44**, 12933 (1991).